metals

MDPI

Article

Effects of Graphite Particle Content and Holding Time on the Microstructure and Mechanical Properties of the Graphite/AZ91D Composite

Xin Gao [1], Kejian Geng [1], Cuicui Sun [1], Suqing Zhang [1,*], Jixue Zhou [1,*], Jianhua Wu [1], Xinfang Zhang [1,2] and Xitao Wang [1,2]

[1] Shandong Provincial Key Laboratory of High Strength Lightweight Metallic Materials, Advanced Materials Institute, Qilu University of Technology (Shandong Academy of Sciences), Jinan 250014, China
[2] School of Metallurgical and Ecological Engineering, University of Science and Technology Beijing, Beijing 100083, China
* Correspondence: zhangsuqing@sdas.org (S.Z.); zhoujx@sdas.org (J.Z.)

Abstract: The effects of Grp (graphite particles) addition and holding time on the microstructure and mechanical properties of the Grp/AZ91D composite were investigated in this work. The results indicated that the distribution of Grp in the matrix was determined by the self-stabilizing mechanism and relationships between the solidifying interface and the particles. Due to the self-stabilizing mechanism, a small amount of Grp would uniformly distribute in the melt alloy, and as the amount of Grp increased, agglomeration would occur. Accordingly, the former would be engulfed by the solidifying interface and the latter would be pushed. With an increased holding time, Grp tended to agglomerate, due to the interfacial reaction that occurred, and as a result, the solidifying interface will push it. The Grp/AZ91D composite with the addition of 1.5 wt.% Grp and a holding time of 15 min obtained grains 30.2 μm in size with a hardness of 89.07 HV, which was a decrease of 83.04% and increase of 35.06% compared to AZ91D, respectively.

Keywords: Grp/AZ91D; self-stabling effect; solidifying interface

check for updates

Citation: Gao, X.; Geng, K.; Sun, C.; Zhang, S.; Zhou, J.; Wu, J.; Zhang, X.; Wang, X. Effects of Graphite Particle Content and Holding Time on the Microstructure and Mechanical Properties of the Graphite/AZ91D Composite. *Metals* **2023**, *13*, 57. https://doi.org/10.3390/met13010057

Academic Editor: Pilar Rey

Received: 17 November 2022
Revised: 22 December 2022
Accepted: 22 December 2022
Published: 25 December 2022

Copyright: © 2022 by the authors. Licensee MDPI, Basel, Switzerland. This article is an open access article distributed under the terms and conditions of the Creative Commons Attribution (CC BY) license (https://creativecommons.org/licenses/by/4.0/).

1. Introduction

Mg alloys are widely used in the aerospace and automobile industries due to their low density, high specific strength, and specific stiffness [1–3]. As one of the most common commercial alloys, AZ91D suffers from the challenge of meeting the requirements of strength and ductility [4,5]. To improve these properties, traditional strengthening strategies can be divided into two parts, namely, micro-alloying and the fabrication of composite materials. Micro-alloying strengthens magnesium alloys by adding rare earth elements [6]. Unfortunately, rare earth resources are expensive and non-renewable, limiting the application of this method [7]. The fabrication of Mg matrix composites can strengthen magnesium alloys by adding an enhancement phase, and traditional magnesium has been incorporated with some ceramic particles, such as SiC, TiC, Al_2O_3, and Mg_2Si [8–11]. In recent years, carbon materials have been used to simultaneously enhance the strength and plasticity, providing high strengthening performance compared to traditional reinforcing phases [12].

However, work on the fabrication of Graphite/AZ91D has been very limited. Rashad et al. successfully fabricated a GNP (graphene nanoplate)/Mg composite material by the powder metallurgy technique, where the addition of 0.2% could significantly improve the mechanical properties [13]. Recently, Liang, et al. fabricated CNT (carbon nano tube)/AZ91D by friction stir processing (FSP), which refined the grains and enhanced the mechanical properties [14]. However, it was very difficult to realize the industrial continuous production by the powder metallurgy method and FSP [15]. Wang, et al. prepared a 5 vol% graphite/AZ91D composite by semi-solid mixing technology, which refined the grain size

and increased the yield strength, tensile strength, and elongation [16]. Wu, et al. fabricated 10% graphite/AZ91D by stir-casting, and found that extrusion at 250 °C leads to the finest grains, and the aspect ratio of graphite particles increases as the extrusion temperature rises [17]. Li, et al. established a thermodynamic method to reveal the formation mechanism of Al4C3 [18]. Composite casting can reduce costs as well as achieve continuous production; therefore, composite casting is an ideal method for composite fabrication. However, research on Grp/AZ91D composites is far from adequate. For example, fabricating high-volume composites using current fabrication methods has proven to be difficult, and the interfacial reaction between the Grp and Mg matrix has not been systematically investigated. Furthermore, we still need to determine and analyze how Grp influences the interfacial reaction and the solidification interface front. In this study, Grp/AZ91D composites were manufactured, which effectively increased the amount of added Grp in the preparation of Grp/AZ91D composite materials, solving the problem of uneven Grp distribution causing defects in tissue performance. Subsequently, the effect of Grp on solidification behavior was investigated and the mechanism was also discussed.

2. Methodology

The Grp/AZ91D composites used in this work were prepared by composite casting. We used a magnesium AZ91 alloy, which consisted of a ternary Mg-9Al-1Zn alloy. A quantity of AZ91D was melted in an electric resistance furnace at 780 °C, after melting isothermally for 30 min. During the casting process using the SF_6 + CO_2 mixture gas as the protective gas, the Grp/AZ91D extrusion billet (using the pressed cake of Grp, AZ91D powders) was introduced. Grp/AZ91D composites with different contents of Grp (0.5 wt.%, 1.0 wt.%, 1.5 wt.%, 2.0 wt.%, 2.5 wt.%) were obtained by changing the addition of the Grp/AZ91D extrusion billet, which was held for 5, 10, 15, and 20 min, at 780 °C. Figure 1 is the schematic of the experimental procedures. Finally, the resulting melt was degassed using SF_6 + CO_2 and poured into a steel mold with a Φ15 mm × 100 mm cavity at 740 °C. The detailed parameters are shown in Tables 1 and 2.

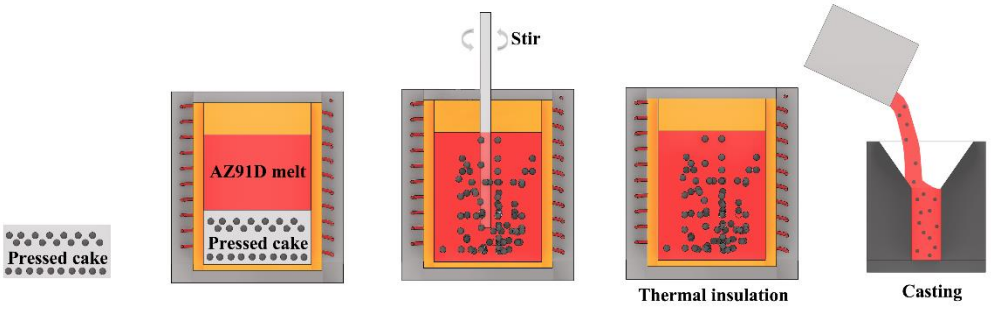


Figure 1. Schematic of experimental procedures.

Table 1. The experiment parameters of the effect of Grp content on Graphite/AZ91D comosites.

Remelting Temperature (°C)	Grp Content (wt.%)	Holding Time (min)	Pouring Temperature (°C)	Protective Gas	Type of Cooling
780	0.5 1.0 1.5 2.0 2.5	15	740	SF6 + CO_2	Air cooling

Table 2. Experiment parameters of the effect of holding time on Graphite/AZ91D composites.

Remelting Temperature (°C)	Grp Content (wt.%)	Holding Time (min)	Pouring Temperature (°C)	Protective Gas	Type of Cooling
780	1.5	0 5 10 15 20	740	SF6 + CO_2	Air cooling

The 10 × 10 × 5 mm^3 specimens were cut from the ingots for metallographic observation and hardness testing. Then, the metallographic specimens were polished and etched using an aqueous solution containing 5 vol.% HNO_3 and observed under an optical microscope (OM) (ZEISS Stemi 2000-c, Oberkochen, Germany) and scanning electron microscope (SEM) (Zeiss EVO M10, Oberkochen, Germany), where the specimens for Grp distribution observations were unetched. We used Image-Pro Plus to measure the grain size, and the metallographic specimens were analyzed using a D/MAX-2500 X-ray diffractometer (XRD) (Rigaku D-Max/2550VB+, Rigaku, Japan). Specimens for TEM (Jeol JEM-2100, Tokyo, Japan) observation were first prepared by grinding–polishing the sample to produce a foil of 50 µm thick followed by punching 3 mm diameter disks and then thinned by ion beam. Similarly, the TEM specimens were preserved in a vacuum can. The hardness was examined by an XHV-1000 hardness tester (Caikang XHV-1000, Shanghai, China), where the average of at least five testing values was taken as the hardness property value.

3. Results

3.1. Effect of Grp Content on the Microstructure

Optical microscopy images of as-cast Grp/AZ91D composites are shown in Figure 2. The as-cast alloys were composed of the α-Mg phase (bright regions), β-$Mg_{17}Al_{12}$ (grey regions), and some small dark particles.

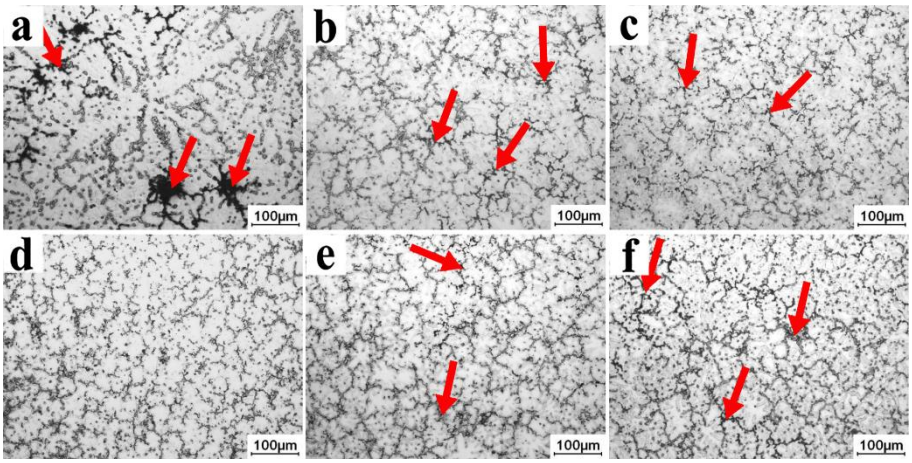


Figure 2. OM micrographs of the Grp/AZ91D composites with different Grp contents: (**a**) 0 wt.%, (**b**) 0.5 wt.%, (**c**) 1.0 wt.%, (**d**) 1.5 wt.%, (**e**) 2.0 wt.%, and (**f**) 2.5 wt.%. (Red arrows: the defects of the composites).

The XRD pattern of the as-cast Grp/AZ91D composites is presented in Figure 3. The results showed that the Grp/AZ91D was composed of the α-Mg phase, β-$Mg_{17}Al_{12}$. When up to 2.0 wt.% Grp was added, the alloy was composed of α-Mg phase, β-$Mg_{17}Al_{12}$, and C phase. Because of the extensive low content of Grp, the peak of the C phase cannot be found below a 2.0 wt.% content of Grp on the XRD pattern. To further confirm the existence of the materials, SEM and EDS were used to analyses the composites.

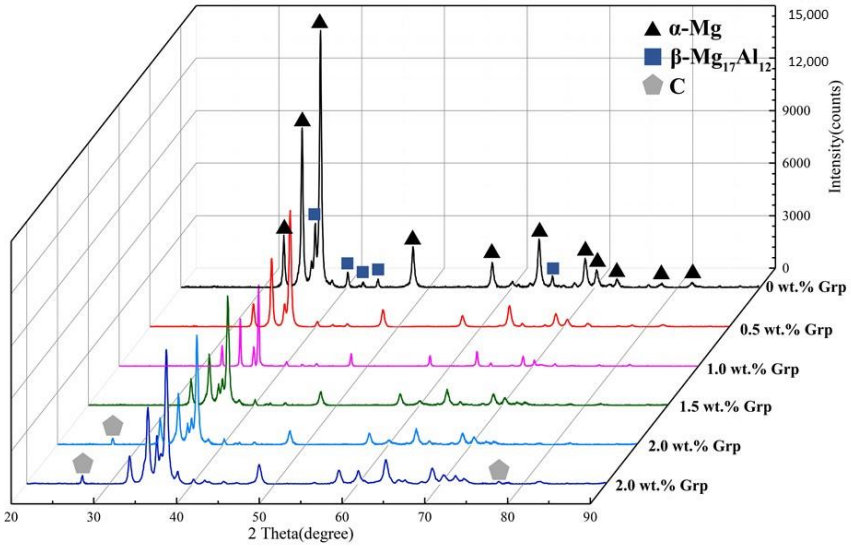


Figure 3. XRD pattern of Grp/AZ91D composites.

Figure 4 shows the SEM image of the Grp/AZ91D specimens, and the results of EDS are presented in Table 3. It indicates that the Grp/AZ91D composite was composed of α-Mg (dark region as shown at point A in Figure 4), β-$Mg_{17}Al_{12}$ (grey fishbone-like region as shown at point B in Figure 4), and a carbon-rich phase (pitch-black particles as shown at point C in Figure 4).

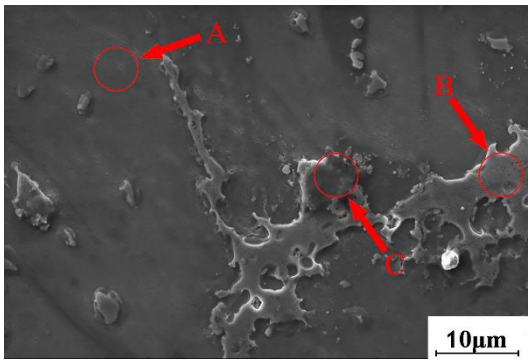


Figure 4. SEM images of 2.0 wt.% Grp/AZ91D.

Table 3. EDS results at different positions shown in Figure 4.

Position	Molar Fraction/%			
	Mg	Al	Zn	C
A	78.39	13.04	0.63	7.94
B	55.98	36.23	1.97	5.82
C	43.13	30.24	0.25	26.38

Figure 2 shows that the addition of Grp could influence the compactness of the Grp/AZ91D composites, and the compactness of the Grp/AZ91D composites was improved by adding an appropriate amount of Grp. The as-cast AZ91D magnesium alloy had many defects, such as shrinkage porosities and porosities (as indicated by the red arrows in Figure 2a). When the addition amount of Grp was less than 1.5 wt.%, the defects gradually decreased with the increasing Grp content (Figure 2a–d), and the defects increased when the Grp content exceeded 1.5 wt.% (Figure 2e,f). With an increase in the Grp content, α-Mg coarse dendrites gradually transformed into equiaxed crystals, and the liquid-phase

feeding ability was enhanced. Grp could refine the grains, which will be elaborated upon further below. As the grain size decreased, the melt was more likely to move, migrate, and replenish the nucleation and solidification zone, effectively improving the solidification defects and improving compactness.

Figures 5 and 6 show the variation of the grain size of Graphite/AZ91D composites with different Grp content. It was obvious that with an increase in Grp content, the grain size first decreased and then increased. According to the quantitative statistical results by Image-Pro Plus software, the grain size decreased from 178.1 μm to 30.2 μm as Grp increased to 1.5 wt.%. However, as shown in Figure 5e,f, when Grp continued to increase, the grains become coarse (2.0 wt.%: 43.2 μm; 2.5 wt.%: 49.3 μm).

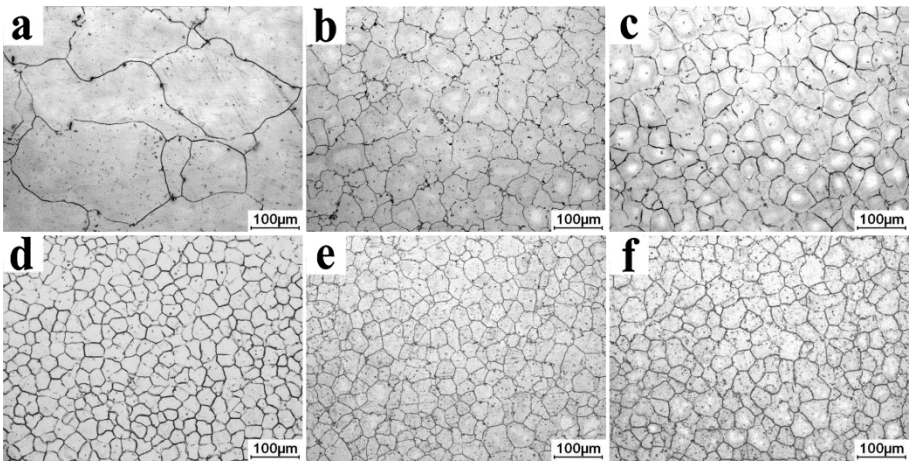


Figure 5. OM micrographs of as-solution Graphite/AZ91D composites with different Grp content: (**a**) 0 wt.%, (**b**) 0.5 wt.%, (**c**) 1.0 wt.%, (**d**) 1.5 wt.%, (**e**) 2.0 wt.%, and (**f**) 2.5 wt.%.

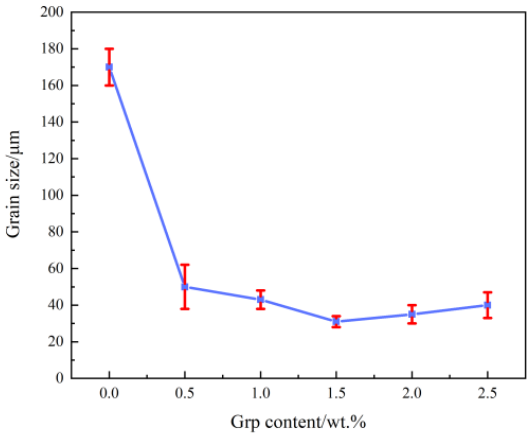


Figure 6. Variation of grain size of Graphite/AZ91D composites with different Grp content.

Figure 7 shows the dispersity of Grp with different Grp contents. We observed that when the Grp content was lower than 1.5 wt.%, Grp was dispersively distributed in the Mg matrix, and became denser with the increasing C_p content (Figure 7a–d). However, when the content was 2.0 wt.%, Grp gradually started to agglomerate (red arrows in Figure 7e) and the size of Grp increased rapidly (red arrows in Figure 7f). At the same time, we found that when the addition of C_p was less than 1.5 wt.%, Grp was mainly distributed in the interior of the α-Mg grains, as shown in Figure 8a,b. When the addition of Grp exceeded 1.5 wt.%, Grp was mainly distributed in the grain boundaries, as shown in Figure 8c,d.

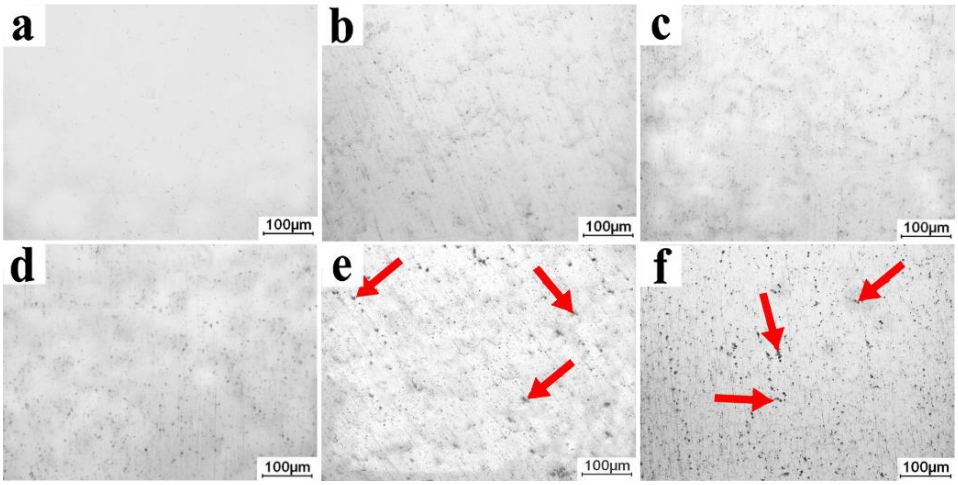


Figure 7. The dispersion of Grp with different Grp contents: (**a**) 0 wt.%, (**b**) 0.5 wt.%, (**c**) 1.0 wt.%, (**d**) 1.5 wt.%, (**e**) 2.0 wt.%, and (**f**) 2.5 wt.%. (Red arrows: the particles of Grp).

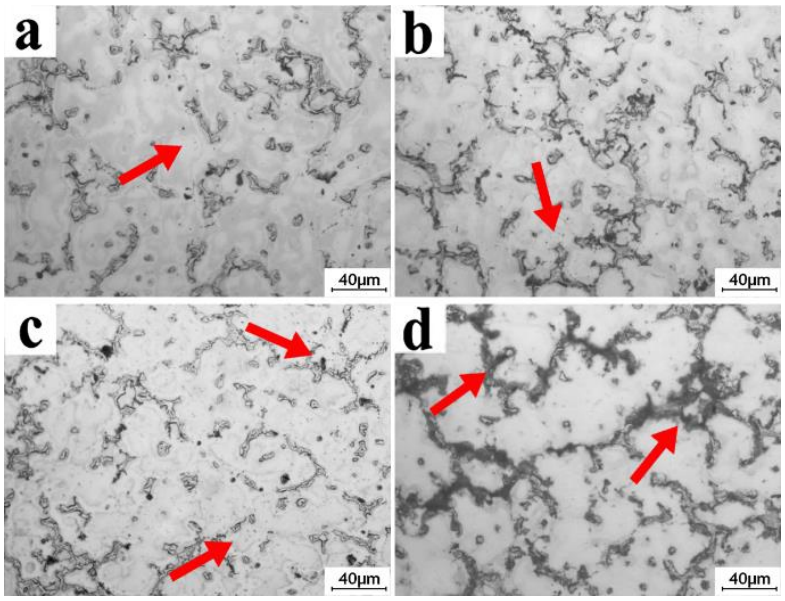


Figure 8. The location of Grp in the Grp/AZ91D composites with different Grp contents: (**a**) 0.5 wt.%, (**b**) 1.5 wt.%, (**c**) 2.0 wt.%, and (**d**) 2.5 wt.%. (Red arrows: the particles of Grp).

3.2. Effect of Grp Content on Hardness Properties

Figure 9 shows the variations in the hardness properties of the Grp/AZ91D composites with different Grp contents. This indicated that the hardness of the Grp/AZ91D composites increased with the increasing Grp content, but when the addition of Grp exceeded 2.0 wt.%, the hardness decreased. Compared to the as-cast AZ91D alloy (65.95 HV), the hardness of the 1.5 wt.% Grp composite (89.07 HV) increased by 35.06%. The evolution of the hardness was consistent with the evolution of the grain size. It indicated that the main reason for the evolution of the hardness was the grain refinement, where too much Grp caused the Grp to agglomerate, and Grp that was too large was found to be more distributed in the grain boundaries, causing the hardness to decrease. However, the grain size was still small, and the reduction in hardness was not significant.

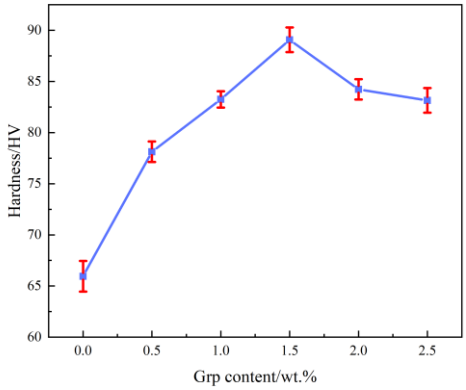


Figure 9. Variations in hardness with Grp content.

3.3. Effect of Holding Time on Microstructure

The compactness of the Grp/AZ91D composites changed with a change in holding time. There were numerous casting defects in the AZ91D alloy, such as shrinkage porosities and porosities (red arrows in Figure 10a). After adding Grp, the casting defects gradually decreased with extended holding time (red arrows in Figure 10b,c). The defects increased with a further extension of time (red arrows in Figure 10e,f), and when the holding time was less than 15 min, the temperature field in the melt was not completely uniform, which caused the viscosity and surface tension of the melt to decrease (Figure 10a–c). In this case, the flowability and filling properties became worse, which caused the porosity of the composite to increase. When the holding time exceeded 15 min, Grp aggregated, resulting in worse flowability (Figure 10d–f).

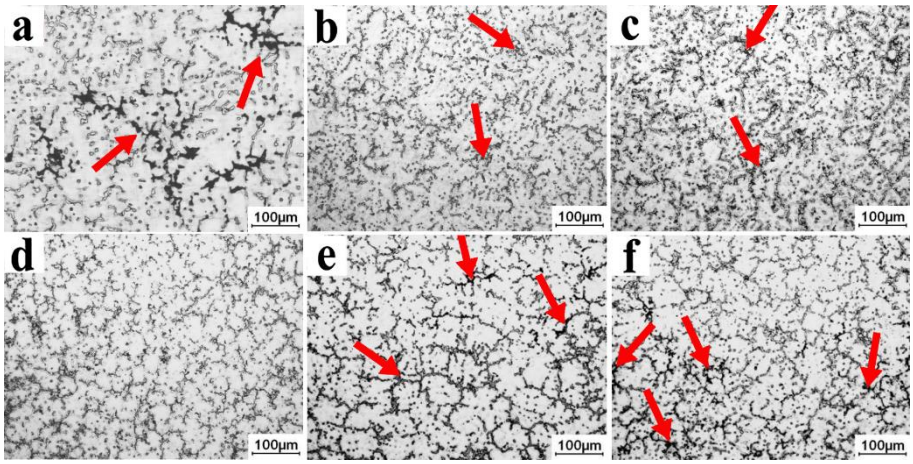


Figure 10. OM micrographs of the Grp/AZ91D composites with different holding times: (**a**) 0 min, (**b**) 5 min, (**c**) 10 min, (**d**) 15 min, (**e**) 20 min, and (**f**) 30 min. (Red arrows: the defects of composites).

Figures 11 and 12 show the variations in average grain size with different holding times, which indicated that the α-Mg grain size gradually decreased with a holding time that was within 15 min. When the holding time was 15 min, the grain size decreased to 30.2 μm; however, when the holding time exceeded 15 min, the grain size gradually increased slightly with additional holding time (Figure 11e,f). The main reason was that C_p pinned the grain boundaries and hindered grain growth.

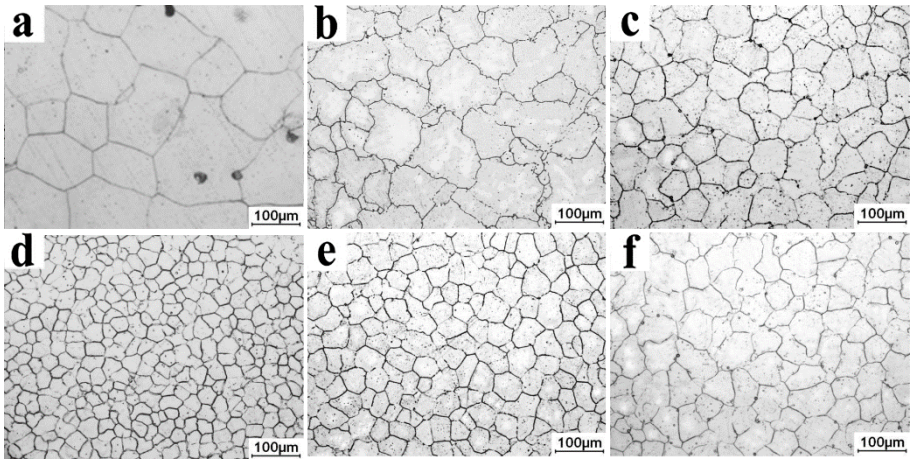


Figure 11. OM micrographs of as-solution Grp/AZ91D composites with different holding times: (**a**) 0 min, (**b**) 5 min, (**c**) 10 min, (**d**) 15 min, (**e**) 20 min, and (**f**) 30 min.

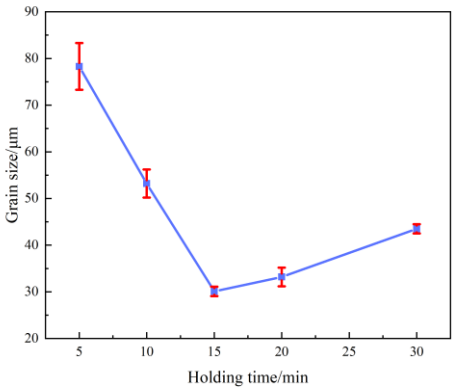


Figure 12. Variation of grain size of Graphite/AZ91D composites with different holding times.

Figure 13 shows the dispersity of Grp in the matrix with an increased holding time, indicating that the size and separation distance of Grp increased as well, and there was a trend of gradual agglomeration, but the distribution of Grp was still dispersed.

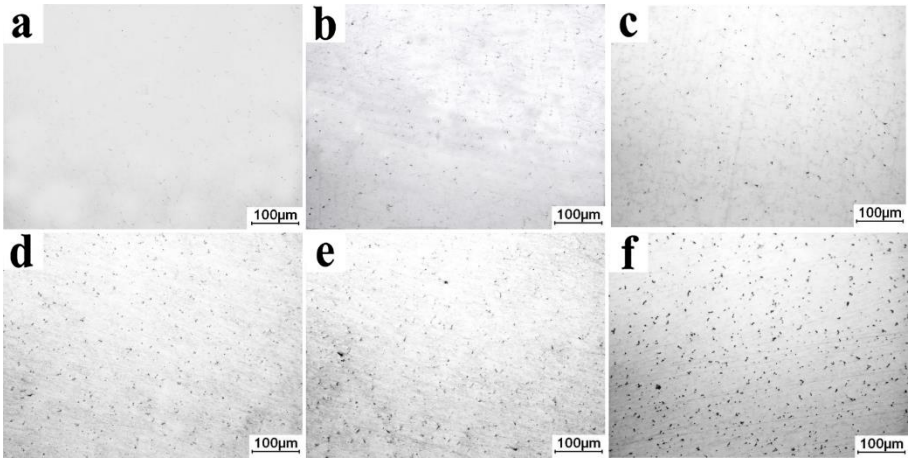


Figure 13. The dispersity of Grp with different holding times: (**a**) 0 min, (**b**) 5 min, (**c**) 10 min, (**d**) 15 min, (**e**) 20 min, and (**f**) 30 min.

Figure 14 shows the location of Grp with different holding times, which indicated that with an extended holding time, the location of Grp changed as well, and Grp was

mainly distributed at the grain boundaries below a holding time of 5 min (red arrows in Figure 14a). With the extended holding time, the distribution of Grp gradually shifted from the grain boundary to the grain interior (red arrows in Figure 14b). However, with an additional extended holding time, Grp was distributed both in the grain interior and in the grain boundaries (red arrows in Figure 14c,d).

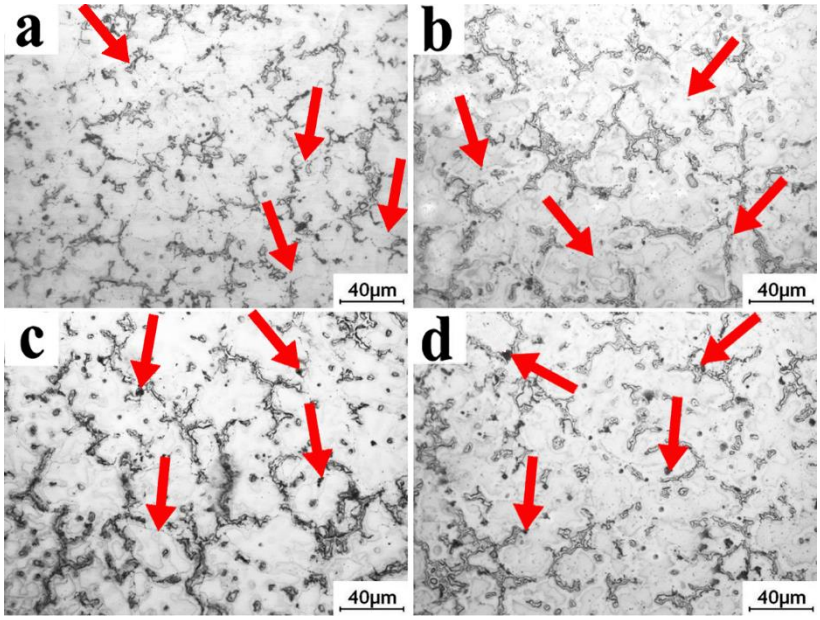


Figure 14. The location of Grp in the Grp/AZ91D composites with different holding times: (**a**) 5 min, (**b**) 15 min, (**c**) 20 min, and (**d**) 30 min. (Red arrows: the particles of Grp).

3.4. Effect of Holding Time on the Hardness Properties

Figure 15 presents the hardness testing at different holding times of Grp/AZ91D. With an extended holding time, the hardness of the composite first increased and then decreased. At 15 min of holding time, the hardness of the composites (89.07 HV) improved by 35.06% compared to the AZ91D alloy (65.95 HV). The change in hardness properties was consistent with the change in grain size within 15 min. With an additional holding time, more interface products were generated, causing the interface to be closely combined, and in this situation, the hardness maintained a relatively high level.

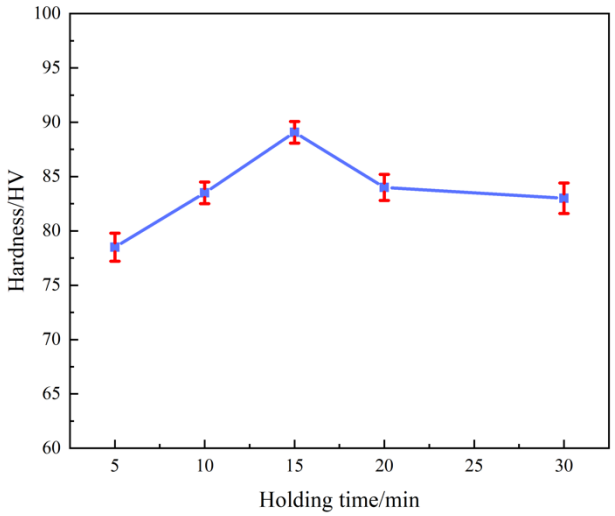


Figure 15. Variations in hardness with holding time.

4. Discussion

4.1. Grain Refinement of Grp

Regarding the refining mechanism of the α-Mg grains by Grp, most studies have shown that Al_4C_3, MgC_2, and Mg_2C_3 will be generated by the Al and C elements in the process of composite preparation at high temperatures as heterogeneous nucleation particles to refine the grain size [19], according to the following equations:

$$4Al + 3C\ (s) \rightarrow Al_4C_3 \quad (1)$$

$$\Delta G_f^\theta\ (J/mol^{-1}K^{-1}) = -71,965 + 13.95T\ (298–933\ K) \quad (2)$$

$$\Delta G_f^\theta\ (J/mol^{-1}K^{-1}) = -88,840 + 32.1T\ (933–2000\ K) \quad (3)$$

$$4Al + 3C\ (s) \rightarrow Al_4C_3 \quad (4)$$

$$\Delta G_f^\theta\ (J/mol^{-1}K^{-1}) = -71,965 + 13.95T\ (298–933\ K) \quad (5)$$

$$\Delta G_f^\theta\ (J/mol^{-1}K^{-1}) = -88,840 + 32.1T\ (933–2000\ K) \quad (6)$$

$$Mg + 2C(s) \rightarrow MgC_2 \quad (7)$$

$$\Delta G_f^\theta\ (J/mol^{-1}K^{-1}) = 27,787 - 9.8T\ (293–923\ K) \quad (8)$$

$$\Delta G_f^\theta\ (J/mol^{-1}K^{-1}) = 15,912 + 3.56T\ (293–1150\ K) \quad (9)$$

$$2Mg + 3C(s) \rightarrow Mg_2C_3 \quad (10)$$

$$\Delta G_f^\theta\ (J/mol^{-1}K^{-1}) = 45,319 - 9.7T\ (293–923\ K) \quad (11)$$

$$\Delta G_f^\theta\ (J/mol^{-1}K^{-1}) = 36,056 + 0.5T\ (923–1150\ K) \quad (12)$$

Figure 16 shows the Gibbs free energy of the formation of different compounds, which indicated that Al_4C_3 was the most stable phase in the Mg-Al-C system. Mg_2C_3 and MgC_2 were both metastable compounds [20]. Under the high temperatures of melting, MgC_2 and Mg_2C_3 easily transformed into other carbon-containing compounds after they were generated [21].

$$4[Al] + 3C(s) \rightarrow Al_4C_3 \quad (13)$$

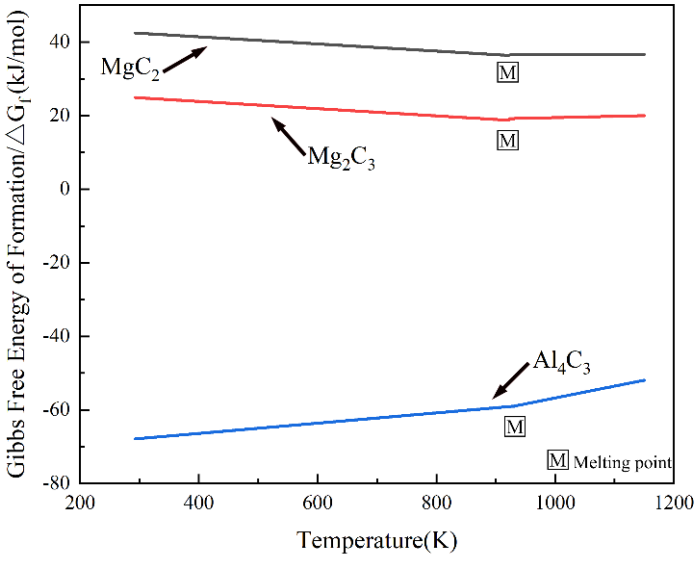


Figure 16. Gibbs free energy of formation of Al_4C_3, MgC_2, and Mg_2C_3.

By calculating the critical reaction temperature at 687 K, the temperature in the smelting process was 1053 K, which was much higher than the critical reaction temperature, $\Delta G < 0$, and the reaction could be carried out [22,23]. According to the grain solidification theory, the necessary condition for the occurrence of heterogeneous nucleation was to find the heterogeneous nucleation particle, finding the grain mismatch degree δ to determine whether the matching index between the heterogeneous nucleation particle and the crystal nucleus was met, as shown in the following formulas:

$$\delta = \frac{d_C - d_N}{d_N} \tag{14}$$

$$\delta = \frac{1}{3}\left[\frac{d_{[uvw]}\cos\theta - d_{[u'v'w']}}{d_{[u'v'w']}}\right] \times 100\% \tag{15}$$

where d_C denotes the interatomic distance of heterogeneous nucleation and d_N is the interatomic distance of α-Mg, where the smaller the value of δ, the more likely that heterogeneous nucleation would occur, according to:

$$\delta = \frac{1}{3}\sum_{\tau=1}^{3}\left[\frac{\left|d_{[uvw]}\cos\theta - d_{[u'v'w']}\right|}{d_{[uvw]}}\right] \times 100\% \tag{16}$$

where $[u'v'w']$ denotes the low-index crystal orientation of crystal nucleus, $[uvw]$ is the low-index crystal orientation of heterogeneous nucleation, and θ is the angle of $[uvw]$ and $[u'v'w']$.

By allowing Al_4C_3 and α-Mg (0001) to coincide, three crystal directions were selected to calculate the mismatch between two crystal faces:

$$= \frac{1}{3} \times \left(2 \times \frac{0.0961\cos 0 - 0.09246}{0.09246} + \frac{0.28847\cos 0 - 0.27739}{0.27739}\right) \times 100\% = 3.999\% \tag{17}$$

The calculated mismatch δ = 3.999% involved matching the requirements of the lattice constant mismatch (<15%) [24]. In conclusion, on the one hand, Al_4C_3 could exist as a heterogeneous nucleation particle of α-Mg, which could improve the nucleation rate of the magnesium matrix composites and achieve the effect of grain refinement, while on the other hand, Al_4C_3 could be extremely easy to adsorb on relatively large Al-Fe rich particles or cluster together due to their high surface energy [18]. In this case, too much addition of Grp or too much holding time would generate a big-sized particle, leading to poor mechanical properties.

Because of the extensive low content of Grp, the diffraction peak cannot be found in the XRD pattern. To further confirm the phase composition of the interface, the interface was observed by transmission electron microscopy (TEM). The results are shown in Figure 17. Figure 17a is a TEM bright-field image of AZ91D/2.0 wt.% Grp with a holding time of 15 min. It can be observed that the AZ91D/2.0 wt.% Grp composite was composed of the bright regions (Figure 17a, C), the interface products (Figure 17a, B), the grey regions (Figure 17a, A), and some black cluster particles (Figure 17a, A). Through TEM diffraction analysis, the grey regions were α-Mg (Figure 17a, A), the black cluster particles were small-sized Grp particles (Figure 17a, A), and the bright regions were β-$Mg_{17}Al_{12}$ (Figure 17a, C). Especially, Figure 17c is the SAED pattern of interface products; the diffraction rings of $(017)_{Al4C3}$, $(110)_{Al4C3}$, $(006)_{Al4C3}$, and $(121)_{Al4C3}$ can be clearly observed which confirmed the generation of Al_4C_3 calculated in the above paragraph.

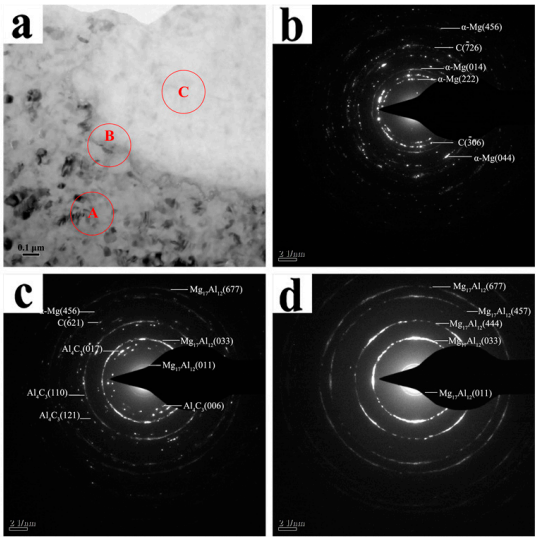


Figure 17. TEM analysis images of the AZ91D/2.0 wt.% Grp with holding time of 15 min: (**a**) TEM bright-field images; (**b**) SAED pattern of the region marked with A; (**c**) SAED pattern of the region marked with B; (**d**) SAED pattern of the region marked with C.

In addition, the dispersed Grp could pin the grain boundaries and hinder further grain growth; however, too much Grp would inhibit the formation of Al_4C_3, and hinder grain refinement. Therefore, when Grp exceeded 1.5 wt.%, the grain size would become large again, and the change in grain size was in accordance with the changes in hardness properties (Figures 6 and 9). In addition, as the grain size decreased, the melt was more likely to move, migrate, and replenish toward the nucleation and solidification zone, effectively reducing the solidification defects and improving Grp/AZ91D compactness (Figures 2b–d and 10a–d).

4.2. Self-Stablizing Effect

Figure 18 illustrates the self-stabilization effect of Grp. Due to the small addition of Grp, the distance between the Grp was large, and the van der Waals forces were weak; therefore, the distribution of Grp was very dispersed (Figures 7a and 18a). When a large amount of Grp was added to the melt, the distance between the Grp decreased (Figure 18b) and the density of the Grp increased significantly, and Grp was more likely to be pulled and agglomerated by van der Waals forces (Figures 7c and 18c). After agglomeration, large particles were more likely to attract small particles that aggregated, which made it difficult to dispersively distribute Grp (Figure 7d,e; Figure 18b,c). With an extended heating time, the energy of the system increased, which resulted in the generation of interfacial products at the edge of Grp. The production of interfacial products could reduce the interfacial free energy and improve the wettability between Grp and the melt, where the contact angle between them would increase [25,26], allowing Grp to merge more easily. Grp gradually gained a greater driving force with an extended heating time, and it diffused more rapidly in the melt. After the merging of Grp, the energy barrier and interfacial energy minimization reached a new balance, due to the increase in the separation distance of Grp. As a result of the poor wettability between the Grp and the melt, the energy barrier decreased after the production of interface products and the probability of particle merging increased (Figures 7f and 18e,f), which made the size of Grp larger.

With an extended holding time, the system energy rapidly increased, which caused Grp to break through the energy barrier more easily and produce interfacial products. In this case, Grp could merge more easily, and the distribution of Grp gradually changed from dispersion to inhomogeneous distribution (Figure 13a–f).

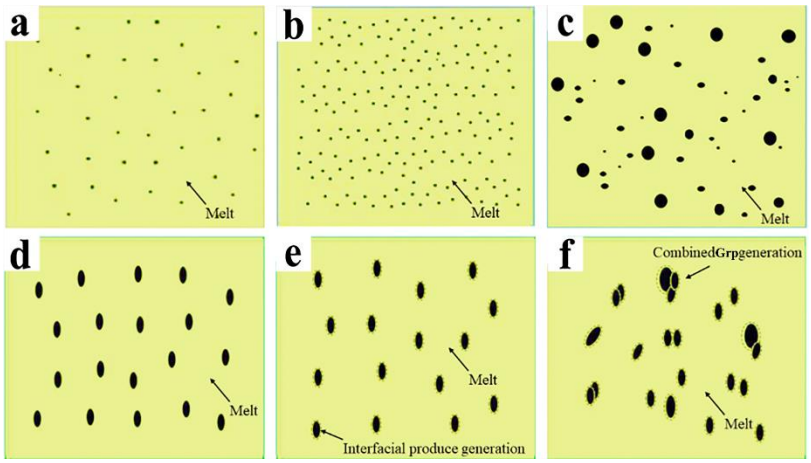


Figure 18. Illustration of the self-stabilization effect of Grp in the melt: (**a**) a small amount of Grp added to the melt, (**b**) a large amount of Grp added to the melt, (**c**) the agglomeration of Grp in the melt, (**d**) Grp added to the melt (enlarged drawing), (**e**) Grp edges producing the interface product, and (**f**) the production of the combined Grp particles.

4.3. The Relationships between the Solidifying Interface and the Particle

The relationship between the solidification interface and the particle could be divided into three parts. Firstly, Grp was swallowed by the interface. Grp was a high heat conductivity particle (Grp 150 w/(m·k) AZ91D 72 w/(m·k)), where the small-sized Grp near the front of the solidifying interface resulted in a temperature with a field that was lower than the surrounding liquid areas. Thus, the growth rate of the solidifying interface was significantly slower compared to other areas. Finally, Grp was engulfed by the solidifying interface (Figures 8a,b, 14b, and 18a). Of note, a holding time that was too short would prevent the system from having enough energy to engulf Grp; therefore, a holding time of 5 min caused Grp to be mainly distributed in the grain boundaries [27] (Figure 14a).

Secondly, Grp was rejected by the interface. According to the following formula, with an increase in Grp content, the melt viscosity increased, and the energy required to push Grp to the interface of Grp agglomeration increased, which reduced the pushing speed at the solid–liquid interface. Therefore, Grp was more likely to be distributed at the grain boundaries, according to:

$$V_e = \frac{\alpha_0 \Delta\delta_0}{12\eta_m \alpha R} \tag{18}$$

$$\alpha = K_p/K_s,\ \alpha_0 = r_p + r_s,\ \Delta\delta_0 = \delta_{sp} - \delta_{1p} \tag{19}$$

where V_e is the critical velocity of solid–liquid interface movement, K_p/K_s is the thermal conductivity ratio of the melt to reinforcing phase, δ_{sp} is the interfacial energy between the alloy and particle in solidification interface, and δ_{1p} is the interfacial energy between the alloy and particle.

The formula of the relationship between the viscosity of the melt (η_m) and the volume fraction of the reinforcing phase (φ) is given by:

$$\eta_m = \eta\left(1 + 2.5\varphi + 10.05\varphi^2\right) \tag{20}$$

where η is the viscosity of AZ91D.

$$V_e = \frac{\alpha_0 \Delta\delta_0}{12\eta_m \alpha R} = \frac{\alpha_0 \Delta\delta_0}{12\alpha R\eta(1 + 2.5\varphi + 10.05\varphi^2)} \tag{21}$$

Based on this formula, with an increase in Grp content, we observed an increase in the melt viscosity and the energy required to engulf the C_p at the solidifying interface. As mentioned above, when the amount of Grp increased, large Grp particles formed. In this

case, the energy was not sufficient to engulf the large particles; therefore, large Grp particles were located in the front of the solidifying interface. As solidification proceeded, more Grp particles were pushed by the solidifying interface, leading to severe agglomeration, which was finally located at the grain boundaries (Figures 8d, 14c and 19b).

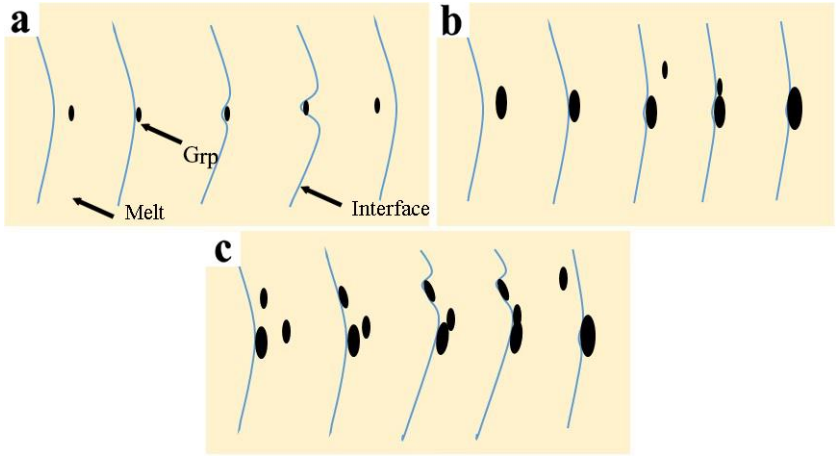


Figure 19. Illustration of the relationship between the solidification interface and the particles: (**a**) Grp swallowed by the interface; (**b**) Grp rejected by the interface; (**c**) Grp swallowed or rejected by the interface.

Thirdly, Grp was swallowed or rejected by the interface, and these two phenomena were in a competing state, where the engulfment mechanism was dominant with a low content of Grp, and the pushing mechanism dominated with high content, as shown in Figures 8c, 14d and 19c. At 30 min of holding time, the system had enough energy to swallow some of the large-sized Grp, but some of the large-sized Grp was still rejected (Figure 14d).

5. Conclusions and Outlooks

(1) A proper technique was achieved, by adding 1.5 wt.% Grp and holding for 15 min. The grain size decreased to 30.2 μm and the hardness increased to 89.07 HV.

(2) According to the solidification theory of interfacial thermal conductivity and the self-stabilizing effect of Grp in the melt, a small amount of Grp was uniformly distributed in the melt and tended to engulf the Grp in the grain during solidification. Adding a large amount of Grp resulted in easy agglomeration, and the distribution in the melt was not uniform; therefore, Grp tended to be excluded from the grain boundaries during solidification.

(3) After the thermodynamic calculations and thermodynamic stability of the products, Al_4C_3 was the easiest phase to generate in the casting process of the Mg-Al alloy melt and the Grp reinforced phase. Al_4C_3, as a heterogeneous nucleation particle, could refine the grains. The thermodynamic conditions of Al_4C_3 formation could be met in the experimental process, improving the nucleation rate of the magnesium matrix composites, and achieving the effect of grain refinement.

(4) Composite casting could fabricate magnesium matrix composites (MMCS) with a low graphite mass fraction. As for MMCS with high graphite mass fraction, traditional composite casting methods would lead to a poor dispersion of graphite, which impeded the desired properties—for instance, good mechanical property and large thermal conductivity, for the various applications. Consequently, it is necessary to probe the general-purpose modifications of graphite materials to achieve well-proportioned dispersion, for the purpose of preparing high-performance materials.

Author Contributions: Writing—original draft, X.G.; study design, X.G., S.Z. and J.W.; funding acquisition, J.Z.; writing—review and editing, C.S. and S.Z.; literature search, K.G.; data collection,

K.G. and J.W.; data analysis, C.S.; project administration, S.Z., J.Z., X.Z. and X.W. All authors have read and agreed to the published version of the manuscript.

Funding: This work was funded by the Youth Innovation and Technology Support Program of Shandong Provincial Colleges and Universities (Grant No. 2020KJA002), and the Shandong Province Key Research and Development Plan (Grant NO. 2021SFGC1001).

Data Availability Statement: All data are available from the corresponding author on reasonable request.

Acknowledgments: The authors wish to express thanks for the financial support from the Youth Innovation and Technology Support Program of Shandong Provincial Colleges and Universities (Grant No. 2020KJA002), and the Shandong Province Key Research and Development Plan (Grant NO. 2021SFGC1001).

Conflicts of Interest: The authors declare that they have no conflict of interest.

References

1. Zhang, S.; Chen, T.; Cheng, F.; Li, P. A comparative characterization of the microstructures and tensile properties of as-cast and thixoforged in situ AM60B-10 vol% Mg_2Si_p composite and thixoforged AM60B. *Metals* **2015**, *5*, 457–470. [CrossRef]
2. Chen, L.Y.; Xu, J.Q.; Choi, H.; Pozuelo, M.; Ma, X.; Bhowmick, S.; Yang, J.; Mathaudhu, S.; Li, X. Processing and properties of magnesium containing a dense uniform dispersion of nanoparticles. *Nature* **2015**, *528*, 539–543. [CrossRef] [PubMed]
3. Chen, X.; Geng, Y.; Pan, F. Research progress in magnesium alloys as functional materials. *Rare Met. Mater. Eng.* **2016**, *45*, 2269–2274.
4. Chen, T.; Huang, L.; Huang, X.; Ma, Y.; Hao, Y. Effects of mould temperature and grain refiner amount on microstructure and tensile properties of thixoforged AZ63 magnesium alloy. *J. Alloy. Compd.* **2013**, *556*, 167–177. [CrossRef]
5. Li, J.; Jiang, Q.; Sun, H.; Li, Y. Effect of heat treatment on corrosion behavior of AZ63 magnesium alloy in 3.5 wt.% sodium chloride solution. *Corros. Sci.* **2016**, *111*, 288–301. [CrossRef]
6. Bettles, C.J. Magnesium powder metallurgy: Process and materials opportunities. *J. Mater. Eng. Perform.* **2008**, *17*, 297–301. [CrossRef]
7. Hao, Y.; Chen, T.; Ma, Y.; Li, Y.; Yan, F.; Huang, X. Some key issues and accesses to the application of magnesium alloys. *Int. J. Mod. Phys. B* **2010**, *24*, 2237–2242. [CrossRef]
8. Gupta, M.; Lai, M.O.; Saravanaranganathan, D. Synthesis, microstructure and properties characterization of disintegrated melt deposited Mg/SiC composites. *J. Mater. Sci.* **2000**, *35*, 2155–2165. [CrossRef]
9. Contreras, A.; Lopez, V.H.; Bedolla, E. Mg/TiC composites manufactured by pressureless melt infiltration. *Scr. Mater.* **2004**, *51*, 249–253. [CrossRef]
10. Habibnejad-Korayem, M.; Mahmudi, R.; Poole, W.J. Enhanced properties of Mg-based nano-composites reinforced with Al_2O_3 nano-particles. *Mater. Sci. Eng. A* **2009**, *519*, 198–203. [CrossRef]
11. Lei, P.; Gang, C.; Zhao, Y.; Huang, K.; Shao, Y. Influence of solution treatment on microstructure and properties of in-situ Mg_2Si/AZ91D composites. *Trans. Nonferrous Met. Soc. China* **2011**, *21*, 2365–2371.
12. Deng, K.; Wang, C.; Nie, K.; Wang, X. Recent research on the deformation behavior of particle reinforced magnesium matrix composite: A review. *Acta Metall. Sin. (Engl. Lett.)* **2019**, *32*, 413–425. [CrossRef]
13. Rashad, M.; Pan, F.; Tang, A.; Muhammad, A.; Muhamad, A. Synergetic effect of graphene nanoplatelets (GNPs) and multi-walled carbon nanotube (MW-CNTs) on mechanical properties of pure magnesium. *J. Alloy. Compd.* **2014**, *603*, 111–118. [CrossRef]
14. Liang, J.; Li, H.; Qi, L.; Tian, W.; Chao, X.; Wei, J. Fabrication and mechanical properties of CNTs/Mg composites prepared by combining friction stir processing and ultrasonic assisted extrusion. *J. Alloy. Compd.* **2017**, *728*, 282–288. [CrossRef]
15. Chen, X.; Li, Q.; Chen, J.; Zhu, L. Microstructure and mechanical properties of Mg-Gd-Y-Sm-Al alloy and analysis of grain refinement and strengthening mechanism. *J. Rare Earths* **2019**, *37*, 1351–1358. [CrossRef]
16. Wang, C.; Deng, K.; Bai, Y. Microstructure, and mechanical and Wear properties of Grp/AZ91 magnesium matrix composites. *Materials* **2019**, *12*, 1190. [CrossRef]
17. Wu, Y.; Wu, K.; Deng, K.; Nie, X.; Wang, X.; Hu, X.; Zheng, M. Effect of extrusion temperature on microstructures and damping capacities of Grp/AZ91 composite. *J. Alloy. Compd.* **2010**, *506*, 688–692. [CrossRef]
18. Li, C.; Yang, S.; Luo, G.; Liao, H.; Du, J. Revealing the nuclei formation in carbon-inoculated Mg-3% Al alloys containing trace Fe. *Materials* **2019**, *12*, 2478. [CrossRef]
19. Chen, H.L.; Schmid-Fetzer, R. The Mg–C phase equilibria and their thermodynamic basis. *Int. J. Mater. Res.* **2012**, *103*, 1294–1301. [CrossRef]
20. Coltters, R.G. Thermodynamics of binary metallic carbides: A review. *Mater. Sci. Eng.* **1985**, *76*, 1–50. [CrossRef]
21. Li, K.; Sun, Z.G.; Wang, F.; Zhou, N.; Hu, X. First-principles calculations on Mg/Al_4C_3 interfaces. *Appl. Surf. Sci.* **2013**, *270*, 584–589. [CrossRef]
22. Viala, J.C.; Claveyrolas, G.; Bosselet, F.; Bouix, J. The chemical behaviour of carbon fibres in magnesium base Mg-Al alloys. *J. Mater. Sci.* **2000**, *35*, 1813–1825. [CrossRef]

23. Viala, J.C.; Fortier, P.; Claveyrolas, G.; Vincent, H.; Bouix, J. Effect of magnesium on the composition, microstructure and mechanical properties of carbon fibres. *J. Mater. Sci.* **1991**, *26*, 4977–4984. [CrossRef]
24. Lu, L.; Dahle, A.K.; StJohn, D.H. Grain refinement efficiency and mechanism of aluminum carbide in Mg–Al alloys. *Scr. Mater.* **2005**, *53*, 517–522. [CrossRef]
25. Presel, F.; Gijon, A.; Hernandez, E.R.; Lacoving, P.; Lizzit, S.; Alfe, D.; Baraldi, A. Translucency of Graphene to van der Waals Forces Applies to Atoms/Molecules with Different Polar Character. *ACS Nano* **2019**, *13*, 12230–12241. [CrossRef] [PubMed]
26. Zhang, A.; Zhao, Z.; Yin, G.; Lin, C. A novel model to account for the heterogeneous nucleation mechanism of α-Mg refined with Al_4C_3 in Mg-Al alloy. *Comput. Mater. Sci.* **2017**, *140*, 61–69. [CrossRef]
27. Shangguan, D.; Ahuja, S.; Stefanescu, D.M. An analytical model for the interaction between an insoluble particle and an advancing solid/liquid interface. *Metall. Trans. A* **1992**, *23*, 669–680. [CrossRef]

Disclaimer/Publisher's Note: The statements, opinions and data contained in all publications are solely those of the individual author(s) and contributor(s) and not of MDPI and/or the editor(s). MDPI and/or the editor(s) disclaim responsibility for any injury to people or property resulting from any ideas, methods, instructions or products referred to in the content.